Chapter 4

Contacting lenses for Antenna-coupled bolometers

4.1 Introduction

The transition from NTD-Ge bolometers to TES bolometers was arguably the key innovation in bolometric receivers over the last decade. The greatest advancement of this decade will likely be remembered as integrating lithographed transmission lines between the antennas and bolometers. Several up-coming CMB experiments, including Berkeley's Polarbear, will use this technology. This chapter begins by contrasting the emerging antenna-coupled devices with more traditional schemes for coupling radiation onto the bolometers. We describe simulations of Polarbear's crossed doubled-slot antenna performed with both Agilent's ADS-momentum and Ansoft's HFSS. These simulations are important for subsequent chapters since the sinuous-antenna design draws it's inspiration from the crossed-double slot antenna. The meat of this chapter is a description of a raytracing script that accounts for the contacting lens in our simulations. This algorithm is well known and has been used by several researchers in the field, but the literature lacks a detailed explanation that this chapter tries to remedy.

All references to measured results in this chapter come from Mike Myers and Kam

Arnold. As previously noted in the acknowledgments, I owe a special thanks to Jen Edwards who pointed out that we must include image currents in the diffraction integral.

4.2 Antenna coupling vs traditional coupling schemes

4.2.1 Horn-Coupled Bolometers

Traditionally, bolometers have coupled to incident radiation with a horn (*Chattopadhyay et al.* [2003]). Often, low-pass "metal mesh" filters on the sky-side of the horns define the upper band edge while waveguide in the back of the horns defines the lower edge. A thermally dissipating structure, such as a spiderweb or PSB (Polarization Sensitive Bolometer), sits a quarter-wavelength above a backshort that maximizes coupling to the detector. A thermistor, such as a TES or NTD-Ge crystal, sits on this released structure to measure the power. Collectively, the thermistor and released structure form the bolometer. Modern CMB experiments that have used this design include QUAD, BICEP-1, APEX-SZ, and SPT.

4.2.2 NIST's Horn-couped Bolometers

NIST has developed a platelette horn-coupled bolometer that replaces the absorbing spiderweb with an orthomode-transducer in the back of the horn (*Yoon et al.* [2009]). The orthomode transducer separates the power into two linear polarizations and couples it onto two separate superconducting microstrip transmission lines. However, before reaching the bolometers, the millimeter waves pass through in-line microstrip band-defining filters which obviate some of the bulky optical filtering that would otherwise be needed in the telescope. This simplifies the required filter stack and helps eliminate ghosting effects often associated with unwanted reflections off the optical filters. Compared to other designs (see sections 4.2.3 and 4.3) that integrate transmission lines between the antenna and bolometers, NIST's is the most traditional because of their choice of a horn antenna.

4.2.3 Caltech/JPL's Array-coupled bolometers

Caltech/JPL has produced an alternative design that replaces the horn with a 12x12 array of slot antennas fed by microstrip lines (*Chattopadhyay et al.* [2007]). Slot antennas are preferred to classic wire dipole antennas because the continuous ground plane can provide RF shielding and also allow for easy integration with microstrip transmission lines. The detectors' beam forming is done entirely in the lithographed antenna array, so the bulky horns with high heat capacity are no longer needed. Aside from this significant difference, the design is otherwise similar to NIST's: the pixels are dual-polarized and integrate band-defining filters between the antennas and detectors.

4.3 Crossed Double-Slot Antenna

At Berkeley, we have developed a design similar to Caltech/JPL's, but with only a 2 element array per polarization in a Crossed-Double-slot Antenna shown in Figure 4.1 (*Myers et al.* [2005]). The first season of Polarbear will deploy a telescope with bolometers coupled to these antennas centered at 150 GHz (*Lee et al.* [2008]). These detectors have 667 μm long slots carved into a 3000Å thick layer of Niobium. Like the competing designs described above, these detectors are also dual polarized with in-line band defining filters. However, to achieve comparable gain to the NIST and Caltech/JPL designs, we have to use a contacting lens that is discussed at length in section 4.4.

4.3.1 Impedance

We simulated the antenna's impedance and beam characteristics in Agilent's Advanced Design Suite (ADS) Momentum. The antenna was drawn as magnetically conducting slots carved into a perfectly conducting ground plane. This plane was at the interface between an infinite half-space of silicon with $\epsilon_r = 11.8$ (on which we fabricate the real detectors) and vacuum. ADS Momentum is a frequency-domain simulator that partitions 2-D planar geometries into tessellating cells called a mesh. It then solves for electric currents in metal
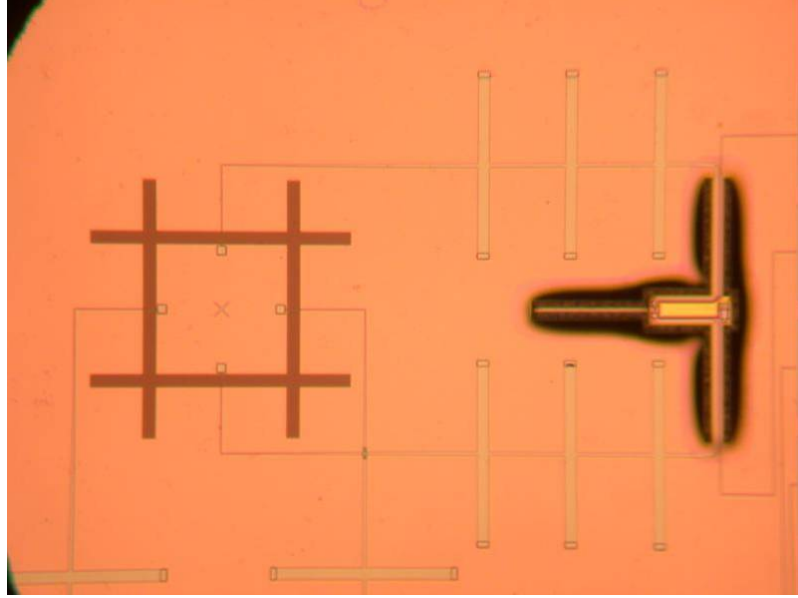
Figure 4.1. Photograph of a Polarbear pixel. The antenna is the "tic-tac-toe" shaped slots in the ground plane at left that couple power to a microstrip transmission line. Similar Bolometers to this one are discussed at length in Chapter 3 and the filter is discussed in Chapter 6

and fictitious magnetic currents in slots by imposing the requirement that electric fields must be normal to a perfect electric conductor and magnetic fields must be normal to magnetic conductors (slots) (*Agilent* [2006]).

One of the primary functions of Momentum and similar simulation packages is to calculate the scattering parameters

$$S_{ij} = \frac{V_i^-}{V_j^+}$$

S_{ij} quantifies what outgoing voltage V_i^- is produced at a port i if a voltage V_j^+ is applied to port j (*Pozar* [2004]). By convention, this definition presumes that each port is normalized to 50 Ω if not otherwise specified. In our simulation, the ports connect to short pieces of microstrip transmission lines that cross the slots and short to the ground-plane on the interior square of the antenna. This is similar to how we couple transmission lines to the slots in our real devices.

The impedance matrix Z_{ij} quantifies what voltage results on a port i when a current flows through port j. The impedance matrix is related to the scattering parameters by:

$$Z_{ij} = (1 + S_{ij})(1 - S_{ij})^{-1}$$

where 1 is an identity matrix (*Pozar* [2004]). This definition assumes that all other ports are open, but in practice, we attach the other ports to transmission lines of matched impedance. The actual input impedance looking into any one port is the ratio of the sum of voltages at that port to the current there. For the crossed-double slot antenna, the input impedance seen looking into port one is:

$$Z_{in} = Z_{11} + \frac{I_2}{I_1}Z_{12} + \frac{I_3}{I_1}Z_{13} + \frac{I_4}{I_1}Z_{14}$$
$$= Z_{11} - Z_{13}$$

where the last three terms represent leakage of power from the other three ports to the first. In practice, little power couples between the two polarizations ($|S_{12}| < -20dB$) and the second and fourth terms can be ignored. The two parallel slots must be driven in phase to construct the proper beam, which means that $I_3 = -I_1$. The simulated input impedance is plotted in Figure 4.2.

This antenna is resonant and has a real impedance near the band center (see Figure 4.2). We operate at the second resonance where the input resistance is a manageable 26 Ω and the total impedance is changing much more slowly than at the first resonance at 71 GHz. The stable impedance provides a 39% fractional bandwidth when matched to an ideal 26 Ω transmission line, in close agreement with other studies on this antenna (*Chattopadhyay and Zmuidzinas* [1998]). The impedances of millimeter wave devices are notoriously difficult to measure, and we have made no attempts to explicitly do so. However, the measured optical throughput of the entire test cryostat with these devices is $\sim 50\%$ over a 30% bandwidth when matched to transmission lines designed for 30Ω impedance. From this success, we suspect that the antenna's actual impedance is close to simulation.
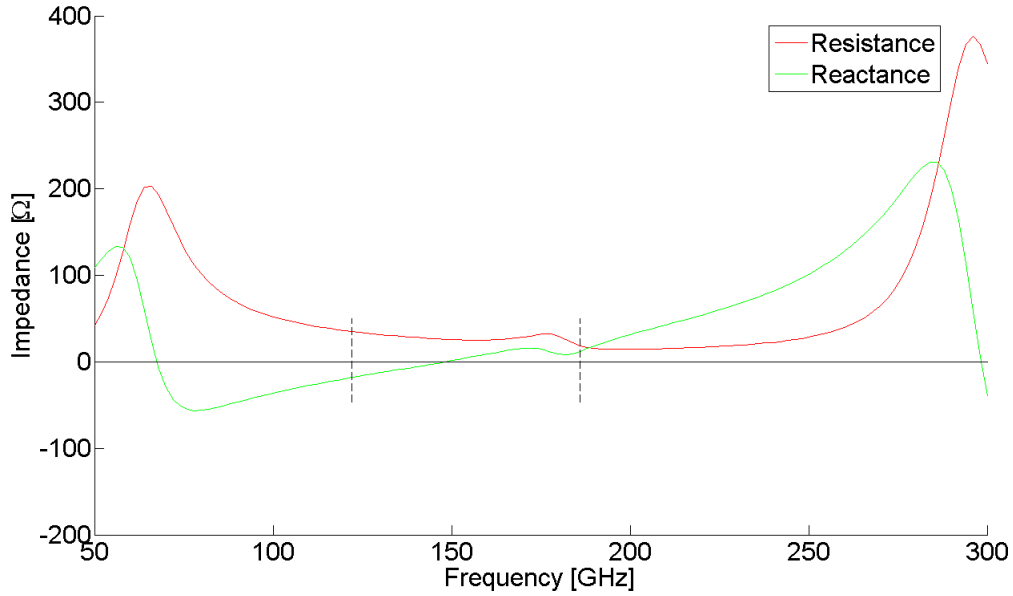
Figure 4.2. ADS simulation of input impedance vs Frequency for the Crossed double-slot antenna. The vertical dashed lines show where the reflection between the antenna and a 26 Ω transmission line rises above -10dB.

4.3.2 Beam Characteristics

Viewed in a time-reversed broadcasting sense, the current in each cell of the surface mesh radiates and the far-field beam pattern is simply the interference pattern from all cells. Thanks to the time-reversal symmetry of Maxwell's equations, the angular sensitivity of the antenna while receiving is identical to this broadcasting beam-pattern.

Figure 4.3 shows the results of this beam simulation. Note that the cross-polarized power as defined in Ludwig's Third Definition (*Ludwig* [1973]), vanishes on axis and only climbs to 1% outside the 10dB edge of the beam. We discuss the beam properites in more detail in Section 4.6 after the contacting lens has been acounted for.

4.3.3 Backlobe Power

If operated in free space, planar antennas have a bi-directional beam pattern with identical power radiated into both directions. However, it is energetically favorable for the antenna on a substrate to radiate predominantly into the substrate side. Depending on
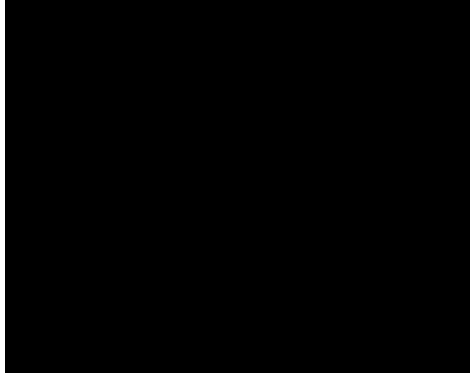
Figure 4.3. ADS simulation of the Crossed Double Slot antenna *without* a lens. The Solid contours are co-polarized power, the dashed are cross-polarized, and the power is on a linear scale normalized to the peak power on boresight.

the antenna geometry, this varies between $\epsilon^{1/2}$ and $\epsilon^{3/2}$, where ϵ is the substrate's relative permittivity.

Part of this effect arises simply because the antenna is driving power into two media in parallel with impedances proportional to $\epsilon_r^{-1/2}$, so the ratio of power into the silicon versus vacuum is $\sqrt{\epsilon_r}$:1. As a result, the Caltech/JPL antenna radiates only 75-80% of it's beam into the forward direction and the lost sensitivity must be recovered with a $\lambda/4$ back-short.

However, the crossed double-slot antennas and sinuous antennas described in later chapters have an even larger power-ratio thanks to the localized currents in the antenna's plane. The electric fields across the slots in the antenna's plane $E(r)$ will have a Fourier Transform $\tilde{E}(k_{xy})$, where k_{xy} resides in the antenna plane. The antenna will radiate waves with wavevectors

$$k_z^2 = \epsilon_r \omega^2/c^2 - k_{xy}^2 \tag{4.1}$$

For these waves to propagate, $k_{xy} < \sqrt{\epsilon_r}\omega/c$; otherwise, the wave exponentially decays with distance (*Goodman* [1968]). The power radiated is
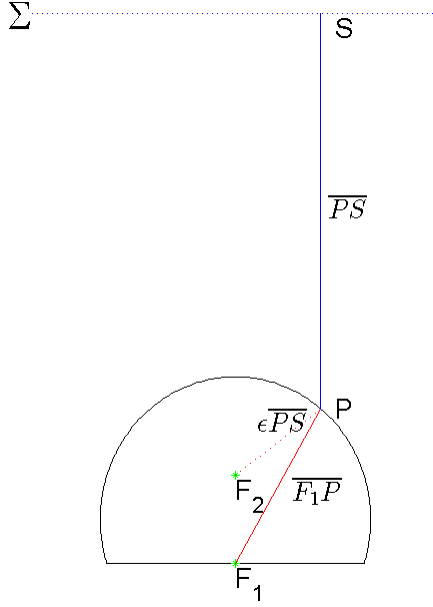
$$P \propto \int dk_{xy}^2 |E(k_{xy})|^2$$

64

Figure 4.4. Rays leaving the antenna at F_1 strike the lens surface at P and travel to points on the directrix plane Σ. If the eccentricity $\epsilon = 1/n$, then the refracted rays will be parallel to the optic axis.

where from Equation 4.1, the area of integration is proportional to ϵ. For a large slot array antenna, the fields are distributed over a wide physical area, so the Fourier transform $E(k_{xy})$ is highly localized and vanishes over most of the integral. However, antennas with wide beams radiating *uniformly* into a half space do not vanish. As a result, the integral adds an extra factor of ϵ to the power ratio, $\epsilon_r^{3/2} : 1$ and only 3% power is in the back-lobe.

In practice, ADS momentum simulations of the double-slot antenna show a beam with a 53° -3dB full-width, 71° at -10dB, and 9% power in the backlobe. This is slightly more than the ideal case, but sufficiently low that we have not worried about installing a back-short.

4.4 Lens Coupling

The Polarbear optics have an f/1.9 and hence need detectors with 30° wide beams at -10dB. The crossed double-slot antenna will not match these optics on it's own. To meet this requirement, we modify our detector beams with a contacting extended hemispherical lens.

An ellipsoidal piece of silicon with the antenna located at one of the foci is an ideal lens for this application (See Figure 4.4). A broadcasting antenna will most efficiently use it's cross-sectional area if the lens transforms the outgoing spherical wavefronts from the antenna within the lens into planar-waves outside the lens. It will accomplish this task if the optical path-length from the antenna at the focus F_1 to any point on the directrix plane Σ is a constant through every point P on the ellipse. Ellipses have the property that the distance $\overline{F_2 P}$ from the upper focus F_2 to any point P on the curve is equal to the ellipse eccentricity ϵ time the distance $\overline{PS}$ from that point P to the directrix Σ (*Apsotle* [1967]). But the sum of the distances from any point on the ellipse to the two foci is a constant, so

$$\text{const} = \overline{F_1 P} + \overline{F_2 P}$$
$$= \overline{F_1 P} + \epsilon \overline{PS} \tag{4.2}$$

If we choose the eccentricity to be the reciprocal of the index of refraction n ($\epsilon = 1/n$), then Equation 4.2 becomes

$$\text{const} = n\overline{F_1 P} + \overline{PS}$$

which shows that the total optical path length from antenna to a plane beyond the tip of the lens is indeed a constant.

In practice, it is difficult and costly to machine a true ellipsoid, so instead we make lenses from extended silicon hemispheres where the antenna is offset from the hemisphere's center by a silicon extension of thickness L_{ext}. The choice $L_{ext}/R = 0.39$ provides an optimal fit to the ellipse with eccentricity $\epsilon = 1/n = 0.29$ for silicon ($n=3.43$) (*Filipovic et al.* [1993]). This geometry is commonly known as a synthesized ellipse and is shown in Figure 4.5.

If a ray strikes a point on the hemisphere at an angle θ from boresight as measured at the spherical center, then it would have departed from the antenna at an angle

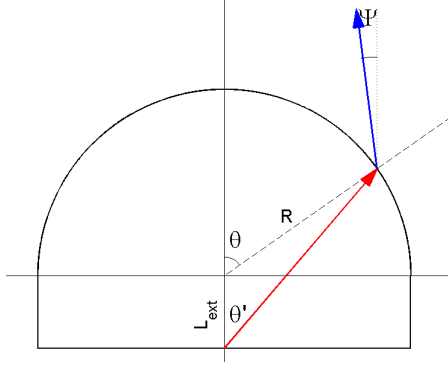$$\theta' = \arctan\left(\frac{R\sin\theta}{L_{ext} + R\cos\theta}\right) \tag{4.3}$$

66

Figure 4.5. The extended hemispherical lens has a radius R and extension L_{ext}. A ray leaving the antenna at θ' from boresight strikes the lens surface at location θ from boresight measured from the lens center. It is refracted into a ray that propagates at an angle Ψ relative to the optic axis.

The refracted ray will propagate away at an angle

$$\Psi = \theta - \arcsin\left(\frac{ng\sin\theta}{\sqrt{1 + 2g\cos\theta + g^2}}\right) \tag{4.4}$$

where $g \equiv R/L_{ext}$. Figure 4.6 shows a plot of refracted vs initially radiated angles for different values of L_{ext}/R. For an ideal ellipsoid, this would be a flat line $\Psi = 0$. The choice of $L_{ext}/R = 0.39$ minimizes deviations of Ψ from zero for all angles out to 47° where total internal reflection starts.

4.5 Raytracing Script

The effects of the lens over the simple crossed double-slot antenna can be simulated with a full 3-D simulator such as Ansoft's frequency-domain High Frequency Structural Simulator (HFSS). HFSS partitions the 3-D space surrounding an antenna into a mesh of cells and directly solves for the electric and magnetic fields in each cell by minimizing the the action associated with those fields. It uses an adaptive-mesh algorithm that iteratively refines the mesh in regions where the field is changing rapidly with each adaptation until the fields satisfy a user-provided convergence criterion.

HFSS simulations of the Polarbear antenna with the lens required roughly 5GB RAM
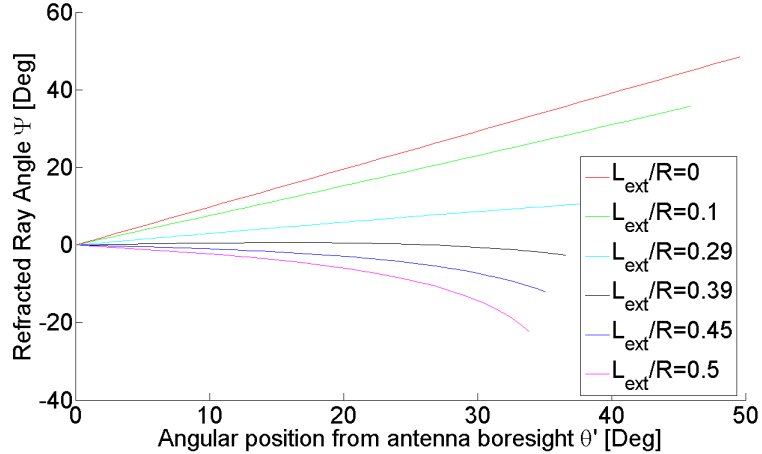
Figure 4.6. Refraction angle Ψ (Equation 4.4) is plotted against angle of radiation measured at the antenna θ' (Equation 4.3) for different lens geometries. Note that an ellipsoidal lens would have $\Psi = 0$ for all θ', so the synthesized ellipse $L_{ext}/R = 0.39$ is a good fit to this ideal

.

to converge. However, the more complicated antennas described in subsequent chapters required a denser mesh in the space surrounding the antenna than the cross-double slot needs. Because of this, the simulations need more RAM than our computer had (32GB). Since these memory requirements cannot be practically met, we instead simulated the log-periodic antennas in ADS where the memory requirements for a 2-D mesh were much lighter. We then accounted for the presence of the lens with a home-made raytracing script (*Filipovic et al.* [1993]) printed in Appendix 1. The following subsections describe the physics behind this algorithm.

Our software assumes that the lens is in the antenna's far field and invokes standard optics principles at that interface. The script exploits time-reversal and calculates beam-patterns as if the antenna were radiating back to the sky. In the far field (Fraunhofer) range, the wavevectors from different radiative elements on the antenna are assumed to be parallel, with phase errors associated with non-parallel rays not exceeding $\pi/8$. This typically begins at a distance of

$$r_{ff} = \frac{2D^2}{\lambda}$$
$$= \frac{2\lambda}{\Omega}$$

where in the D^2 is the effective area of the antenna and the antenna theorem for a single-moded antenna has been invoked in the second line (*Collin* [1985]). Waves at 150GHz in silicon have $\lambda = 0.58$mm, so the far field for Polarbear's crossed double-slot antenna begins at $r_{ff} = 1.99$mm. Since the equator of the 6.35mm diameter lens hemisphere is 3.4mm away from the antenna (for a synthesized ellipse), the lens surface is safely within the far-field and our algorithm is justified. The measurements and simulations of the log-periodic antennas in subsequent chapters used a lens with a 14mm diameter, so the algorithm was also justified for them as well, even at frequencies as low as 70GHz.

4.5.1 Refraction at the lens surface

Our code partitions the lens surface into a tessellating mesh of surface patches and interpolates the ADS-simulated fields at the patches' angular locations (θ', ϕ) measured at the antenna . If the lens's hemispherical surface has unit normal vectors $\hat{\mathbf{n}}$ and the outgoing rays strike with incident unit wavevectors $\hat{\mathbf{k}}$, then the refracted field's unit wavevectors (outside the lens) $\hat{\mathbf{k}}^{\mathbf{t}}$ are simply a rotation of the incident within the Plane Of Incidence (POI) by an angle of

$$\Psi = \arcsin(n_{lens}\sin(\hat{\mathbf{k}} \cdot \hat{\mathbf{n}})) - \hat{\mathbf{k}} \cdot \hat{\mathbf{n}}$$

towards boresight. The vectors $\hat{\rho_{\perp}} \equiv \hat{\mathbf{n}} \times \hat{\mathbf{k}}$ and $\hat{\rho_{\parallel}} \equiv \hat{\rho_{\perp}} \times \hat{\mathbf{k}}$ are respectively perpendicular to and within the POI and form a local basis with the vector $\hat{\mathbf{k}}$. The refracted wavevector in this basis is:

$$\hat{\mathbf{k}}^{\mathbf{t}} = \cos(\Psi)\hat{\mathbf{k}} + \sin(\Psi)\hat{\rho}_{\parallel}$$

The incident fields can also be written in this basis, where the field components normal to the plane of incidence $(\mathbf{E} \cdot \hat{\rho_\perp})\hat{\rho_\perp}$ and $(\mathbf{H} \cdot \hat{\rho_\perp})\hat{\rho_\perp}$ are eigenvectors of refraction, only modified in magnitude by their respective transmission coefficients $\tau_\perp$ and $\tau_\parallel$. The transmitted field components within the POI are

$$\mathbf{E}_\parallel{}^t = \eta \mathbf{H}_\perp{}^t \times \hat{\mathbf{k}}^t$$
$$= \tau_\parallel E_\parallel^o (\cos(\Psi)\hat{\rho}_\parallel - \sin(\Psi)\hat{\mathbf{k}})$$
$$\mathbf{H}_\parallel{}^t = \frac{1}{\eta}\hat{\mathbf{k}}^t \times \mathbf{E}_\perp{}^t$$
$$= -\tau_\perp H_\parallel^o (\cos(\Psi)\hat{\rho}_\parallel - \sin(\Psi)\hat{\mathbf{k}})$$

where η is the impedance of free space. These components rotate by Ψ around the $\hat{\rho_\perp}$ axis, much like $\hat{\mathbf{k}}$.

For a lens without a coating, the transmission coefficients are given by the Fresnel Equations that require the tangential components of the electric and magnetic fields to be continuous across the interface:

$$\tau_\perp = \frac{2\cos\theta_i \sin\theta_t}{\sin(\theta_i + \theta_t)}$$
$$\tau_\parallel = \frac{2\cos\theta_i \sin\theta_t}{\cos(\theta_i - \theta_t)\sin(\theta_i + \theta_t)}$$

4.5.2 Anti-reflection Coating

For a lens with an anti-reflection coating, the tangential field components must be continuous at *both* the inner and outer interfaces of that film. Assuming that the film is roughly planar, these requirements result in a set of equations relating the fields just inside the lens $[E_o H_o]$ to those just outside $[E_t H_t]$ through the transfer matrix $\mathcal{M}$:

$$\begin{pmatrix} E_o \\ H_o \end{pmatrix} = \begin{pmatrix} \cos(k_o h) & i\sin(k_o h)/\Upsilon_{ar} \\ i\Upsilon_{ar}\sin(k_o h) & \cos(k_o h) \end{pmatrix} \begin{pmatrix} E_t \\ H_t \end{pmatrix} \equiv \mathcal{M} \begin{pmatrix} E_t \\ H_t \end{pmatrix} \tag{4.5}$$

where $h = nd\cos(\theta_{\mathrm{ar}})$ is related to the film with thickness d and angle of incidence θ_{ar} and the admittance Υ_{ar} depends on the polarization of the mode under consideration

$$\Upsilon_{\mathrm{ar}} = \frac{n_{\mathrm{ar}}}{\eta} \begin{cases} \cos(\theta_{\mathrm{ar}}) \text{ for TE modes} \\ \sec(\theta_{\mathrm{ar}}) \text{ for TM modes} \end{cases}$$

An elementary description of the lens would sum the fields associated with multiple rays reflecting through the coating. However, this approach would be an onerous when considering the multilayer films discussed in Section 7.5. The transfer-matrix formulation is more powerful because multiple coatings can be modeled by simply multiplying transfer matrices to produce one effective matrix (*Born and Wolf* [1999]). The electric field transmission coefficient is

$$\tau = \frac{2\Upsilon_o}{\Upsilon_o \mathcal{M}_{11} + \Upsilon_o \Upsilon_{\mathrm{lens}} \mathcal{M}_{12} + \mathcal{M}_{21} + \Upsilon_{\mathrm{lens}} \mathcal{M}_{22}} \tag{4.6}$$

where the admittance for the free space and lens materials are defined in a similar way as above, but independent of polarization:

$$\Upsilon_{\mathrm{lens},0} = \frac{n_{\mathrm{lens,o}}}{\eta} \cos(\theta'^{,t})$$

The wavevector and fields within the plane of incidence will still rotate by the angle given above despite the extra film layer(s), so that part of the algorithm from uncoated lenses carries over for lenses with a coating.

4.5.3 Deviations from an ideal anti-reflection coating

Our software assumes that the coatings are planar and of uniform thickness across the hemisphere. However, the coatings are not planar, which can give rise to field alignment errors. Additionally, the coatings should be tapered in thickness because a uniform thickness creates phase errors in the film off boresight that can degrade it's properties. In the following two subsections, I argue that these are not practical concerns for our application.
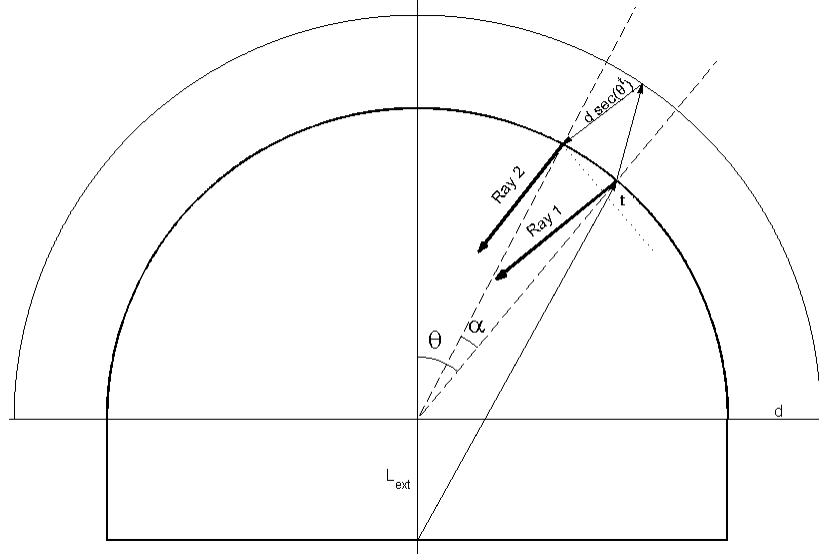
Figure 4.7. Cross sectional Cartoon of the lens with a single layer coating with an exaggerated thickness. The two reflected rays Ray 1 and Ray 2 must destructively interfere for the coating to work. However, the rays are not parallel; one is rotated with respect to the other by α. On boresight, Ray 2 will have a 90° phase shift relative to Ray 1 from it's extra travel of $2d$ through the film. But off boresight, Ray 2 travels an extra $2d(\sec\theta^t - 1)$ while Ray 1 travels an extra $t = 4d\tan\theta^t\sin\theta^t$

Field Alignment Errors

For radiation normally incident on a flat AR-film, a $\lambda/4$ thickness will ensure that the multiple rays reflected from the interface will be 180° out of phase and destructively interfere. Additionally, a film index that is the geometric mean of the inner and outer media's will ensure the ray's powers are matched in order to maximize this interference. But this cancellation happens because the reflected fields from the beams are parallel. While this is guaranteed for a flat coating where the two surfaces are parallel planes, it is not always the case when the two surfaces are concentric spheres. The reflected beams will still make the same angle with respect to the local normal vectors at the inner surface. However, those radial normal vectors themselves are not parallel, so the second beam will be rotated from the first by an angle of

$$\alpha \approx 2\arcsin\frac{d}{R}\frac{n_{lens}}{n_{ar}}\frac{\sin\theta}{\sqrt{1 + 2R/L_{ext}\cos\theta + (R/L_{ext})^2}}$$
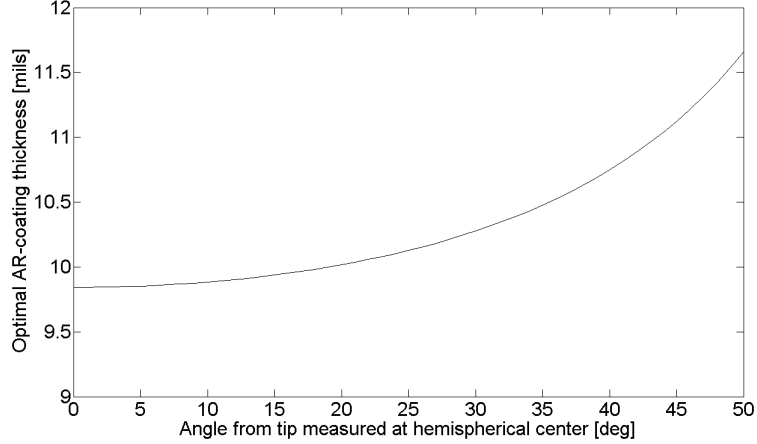
Figure 4.8. Ideal AR-coating thickness vs angle on the hemisphere. This would compensate for phase errors between the reflected beams off boresight. It is unlikely that we could actually make this compensation since the film thickness varies by less than 2 mils while a highly skilled machinist will often achieves 1 mil tolerances.

.

where d is the film thickness, R the inner radius, and θ the angle at the surface relative to the hemispherical center. For the polarbear detectors, this angle is no greater than 6.6^o, which means that the power of the mis-aligned field components in the plane of incidence is 0.004% of the total field power at the beam's -10dB contour. This error is negligable.

Phase Errors

We have only fabricated AR-coating films of uniform thickness. On boresight, the $\lambda/4$ thick film generates a $\pi/2$ phase delay between the first and second beams in Figure 4.7. Off axis, the second ray is delayed by $2n_{ar}d\sec\theta^t$ because it must travel further. However, the first ray *also* experiences an additional delay of $4n_{lens}d\tan\theta^t\sin\theta^t$. Surprisingly, the first ray's phase-delay is longer than the second ray's and to compensate, the film must be made thicker at large angles from boresight.

For a stycast coating with $n = 2$, this coating must be 9.84 mils thick. However, the film thickness is only 11.3 mils at the angles where Total-internal reflection starts (see Figure 4.8), which is likely within the machine tolerances of any AR coating that we attempt to mold.

73

4.5.4 Diffraction through the lens

The antenna beam also diffracts through the lens. A vectorial diffraction theory is needed in this case to properly account for the polarization properties of the antenna-lens system. The vector Kirchhoff integral relation follows from a simple application of Green's Second Identity:

$$\mathbf{E}(\mathbf{x}) = \oint_{S'} [i\omega(\mathbf{n}'\times \mathbf{B}_t)G + (\mathbf{n}'\times \mathbf{E}_t) \times \nabla'G + (\mathbf{n}'\cdot \mathbf{E}_t)\nabla'G]da' \tag{4.7}$$

This equation quantifies Huygen's wavelet principle; it describes how a set of fields $\mathbf{E}_t$ and $\mathbf{B}_t$ with known values on the closed surface S' (which has a normal vector $\mathbf{n}'$) interfere to created a diffracted field $\mathbf{E}(\mathbf{x})$ (*Jackson* [1998]). All of the information relevant to the far field is contained in the fields on the surface, regardless of what currents are interior to that surface. The subscript t is a reminder that fields are those transmitted through the lens surface as determined by the refraction equations of the previous subsection.

At an observation point $\mathbf{x}$ far from the lens surface, the Greens function is

$$G(\mathbf{x}, \mathbf{x}') = \frac{e^{ikr}}{4\pi r}e^{-i\mathbf{k}\cdot\mathbf{x}'}$$

and it's gradient is $\nabla'G = -i\mathbf{k}\,G$. Inserting this into Equation 4.7 and replacing the magnetic induction $\mathbf{B}$ with the magnetic field $\mu\mathbf{H}$ yields

$$\mathbf{E}(\mathbf{x}) = \frac{ike^{ikr}}{4\pi r}\oint_{S'} e^{-i\mathbf{k}\cdot\mathbf{x}'}[\eta(\mathbf{n}'\times \mathbf{H}_t) - \hat{r} \times (\mathbf{n}'\times \mathbf{E}_t) - \hat{r}(\mathbf{n}'\cdot \mathbf{E}_t)]da' \tag{4.8}$$

where η is impedance of free space and the wavevector $\mathbf{k}$ was assumed to be propagating radially outward.

Engineers often substitute fictitious electric and magnetic surface currents and charges over the surface S' into this equation:

$$\mathbf{J}_E = \mathbf{n}' \times \mathbf{H}_t \tag{4.9}$$

$$\mathbf{J}_M = -\mathbf{n}' \times \mathbf{E}_t \tag{4.10}$$

$$\rho_E = \epsilon_o \mathbf{n}' \cdot \mathbf{E}_t \tag{4.11}$$

(*Collin* [1985]). In addition to beautifying otherwise ugly equations, these aid intuition by acting as tangible sources that re-radiate into a scattered wave. The spherical components of the far-field diffracted wave in Equation 4.8 are:

$$E_r = \frac{ike^{ikr}}{4\pi r} \oint_{S'} e^{-i\mathbf{k}\cdot\mathbf{x}'} [\eta \hat{r} \cdot \mathbf{J}_E - \rho_E/\epsilon_o] da' \tag{4.12}$$

$$E_\theta = \frac{ike^{ikr}}{4\pi r} \oint_{S'} e^{-i\mathbf{k}\cdot\mathbf{x}'} [\eta \hat{\theta} \cdot \mathbf{J}_E + \hat{\phi} \cdot \mathbf{J}_M] da' \tag{4.13}$$

$$E_\phi = \frac{ike^{ikr}}{4\pi r} \oint_{S'} e^{-i\mathbf{k}\cdot\mathbf{x}'} [\eta \hat{\phi} \cdot \mathbf{J}_E - \hat{\theta} \cdot \mathbf{J}_M] da' \tag{4.14}$$

The first term is identical to the second in the brackets of 4.12, so E_r vanishes as expected for a transverse traveling wave. The remaining components (Equations 4.13 and 4.14) can be written in terms of electric and magnetic vector potentials ($\mathbf{N}$ and $\mathbf{L}$):

$$E_\theta \propto \eta \mathbf{N} \cdot \hat{\theta} + \mathbf{L} \cdot \hat{\phi}$$

$$E_\phi \propto \eta \mathbf{N} \cdot \hat{\phi} - \mathbf{L} \cdot \hat{\theta}$$

where

$$\mathbf{N} \equiv \oint_{S'} e^{-i\mathbf{k}\cdot\mathbf{x}'} \mathbf{J}_E da'$$

$$\mathbf{L} \equiv \oint_{S'} e^{-i\mathbf{k}\cdot\mathbf{x}'} \mathbf{J}_M da'$$

The integral must be performed over a closed surface, and our code closes this surface by including an image hemisphere below the ground plane with image currents on that

imaginary-surface. To ensure that all electric fields at the perfectly conducting ground plane remain normal to that surface, the electric-current image components perpendicular to ground must be the in the same direction as the original, while the components parallel to ground must be in the opposite direction (see Figure 4.9(a)). The opposite is true for the magnetic-current images to ensure that magnetic-fields are tangential to the ground-plane (see Figure 4.9(b)). The code does not integrate over the cylindrical extension surface since it starts 69° from boresight in a synthesized ellipse, and the bare antenna power is well below 1% of that at boresight in that region.

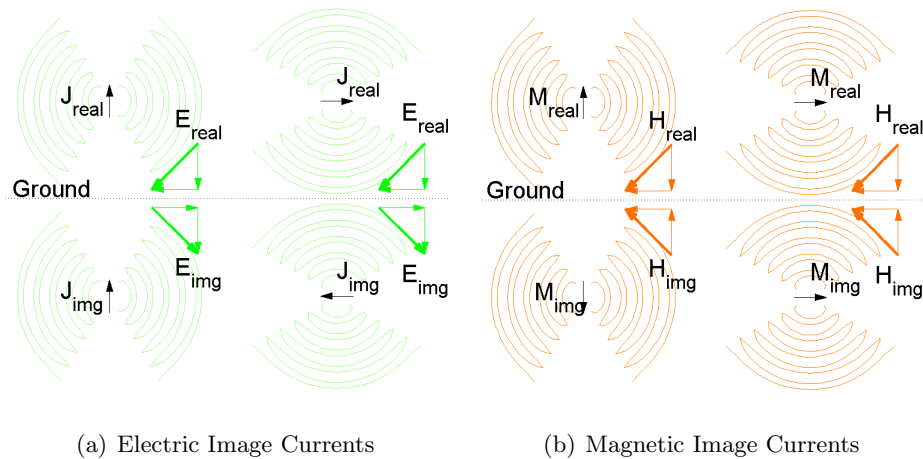(a) Electric Image Currents   (b) Magnetic Image Currents

Figure 4.9. Boundary conditions for image current construction. Real and image currents are black vectors, green curves and arrows are electric fields **E**, and orange curves and arrows are magnetic fields **H**. The field contours are for far-field dipole radiation; any antenna's far-field is the superposition of these fields. The components of the fields at a point on the ground plane are broken into components parallel and perpendicular to ground to make clear how the choice of image current guarantees that the tangential electric fields and normal magnetic fields vanish there.

4.6   Comparison to HFSS simulations

To vet our algorithm, we compared the results of computations against HFSS's full 3-D simulations, the geometry of which can be seen in Figure 4.10. The slot antenna is located near the origin on the x-y plane and has a geometry identical to the one described in the ADS simulations. We excited the slot parallel to the x-axis with a lumped voltage across the slot on a line along the y-axis. The lens models the ones to be used in the Polarbear
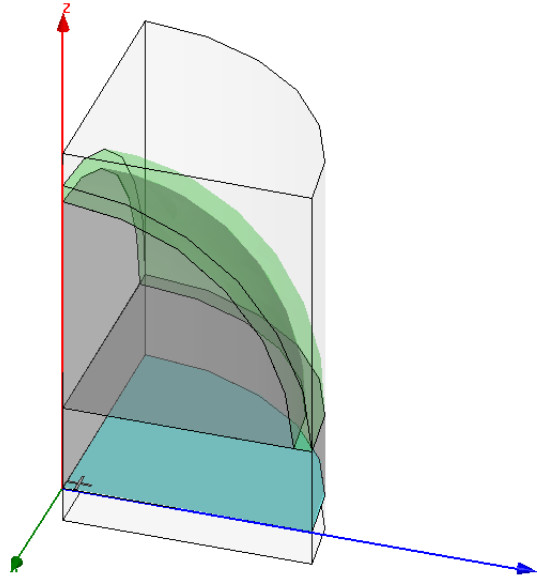
Figure 4.10. Layout for HFSS simulation. The yz-plane (facing the viewer) is a "Perfect-H" symmetry plane, while the xz-plane facing left is a "Perfect-E". All other external surfaces are perfect radiation absorbers.

experiment. It is silicon with a relative permittivity of 11.8, a diameter of 6.35mm (1/4 inch), and an elliptical extension of 1.24mm. The AR-coating (shown in green) is a 0.25mm film of stycast-2850, with a relative permittivity of 4. It is a quarter-wavelength thick at 150GHz.

To reduce the memory requirements of the simulation, we only simulated 1/4 of the antenna in HFSS and exploited the four-fold symmetry of the antenna by use of symmetry planes. The x-z plane is a "perfect-E" symmetry plane that force the electric fields there to be normal. This symmetry plane also ensures that there will be an image-source with opposite polarity across the image slot parallel to the x-axis. Similarly, the y-z plane is a "perfect-H" symmetry plane that forces Electric fields there to be tangential to that plane. The fields would have these properties in a simulation of the entire lens, but with this geometry, only 8Gb of RAM were required and our computer completed a simulation of a single frequency in under 20 minutes.

The beams from the two simulations are shown separately in the side-by-side contour plots in Figure 4.12. The beams are also co-plotted as cuts in Figure 4.11. The E-plane is
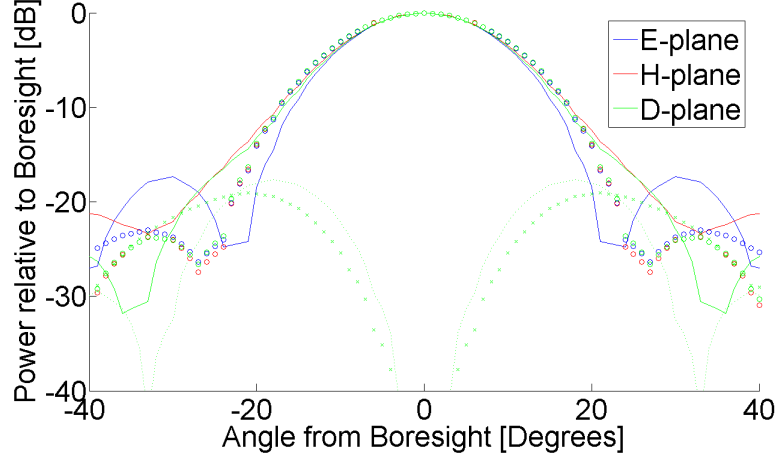
Figure 4.11. Cuts of HFSS and ADS-lensed simulations. Solid and Dashed lines are co and cross polarized power from HFSS. Points marked 'o' and 'x' are co and cross polarized power from ADS and raytracing.

the axis parallel to the polarization, H-plane is perpendicular, and the D-plane is at a 45° between them. The two simulations produce beams with comparable features at high powers (above -10dB), but diverge at lower powers. In particular, the ADS-raytracing calculates significantly lower side-lobe and cross-pol levels than HFSS.

Table 4.1 summarizes the beam properties from the two simulations. In addition to the parameters already discussed, it also cites ellipticity, gain, and beam waist. The ellipticity is defined as

$$e = \frac{a - b}{a + b} \tag{4.15}$$

where a and b are the angular widths of the semi-major and semi-minor axis at a contour of a specific power. Gain is the ratio of antenna power on boresight to that from isotropic radiator; it quantifies how focused the beam is. The beam waist is the radius of the $1/e^2$ power contours where the beam is most narrow. We infer it from the $1/e^2$ half-angle angle in the far field:

$$w_o = \frac{\lambda}{\pi \theta_{FF}} \tag{4.16}$$

78

The beam waists are roughly 70-80% of the lens radius, as our UCSD collaborators have previously measured for a synthesized ellipse. For comparison, a uniformally illuminated aperature of 6.35mm diameter would have it's first Airy-ring diffraction minimum at an angular diameter of 45°.

Table 4.1. Antenna Beam Properties

Parameter	ADS-Raytrace	HFSS
E-plane -3dB Width [Deg]	19.7^o	18.0^o
H-plane -3dB Width [Deg]	19.9^o	18.6^o
E-plane -10dB Width [Deg]	34.5^o	31.5^o
H-plane -10dB Width [Deg]	34.7^o	34.9^o
E-plane Beam Waist [mm]	2.24	2.47
H-plane Beam Waist [mm]	2.22	2.25
Peak Side-lobe Levels [dB] (E-plane)	-22.0	-17.3
Peak cross-pol [dB] (D-plane)	-19.1	-17.6
Gain [dB]	13.7	15.4
Ellipticity	0.5%	1.6%

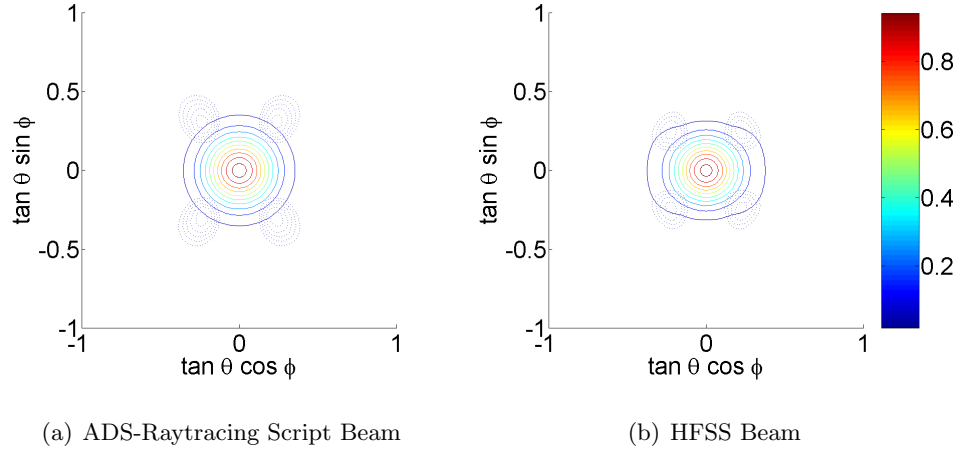(a) ADS-Raytracing Script Beam   (b) HFSS Beam

Figure 4.12. Contour plots of ADS simulation modified with the raytracing script (left) and from HFSS simulations (right). Solid lines are co-polarized power, dashed are cross-polarized, and the power is on a linear scale. They agree in many of their course features, but not in the fine details (See table). Notice that these are half as wide as the un-lensed beam in Figure 4.3.

4.7 Conclusions

We described the double-slot antenna in detail since it motivates the antenna development in subsequent chapters and because it is an established yet simple design that we used to test our raytracing script. We have also motivated the use of contacting lenses to boost the gain of a detector's antenna so we can match it to a telescope's optics. Our raytracing algorithm seems to produce lens-coupled antenna beams that agree with the industry-standard HFSS at the 10% level, but differs in the finer details. We consider these differences in later chapters when we compare results from this model against our measurements.